

Diffeomorphic Atlas Estimation using Geodesic Shooting on Volumetric Images

François-Xavier Vialard^{1,*}, Laurent Risser^{1,2,*}, Daniel Rueckert², Darryl D. Holm¹

¹Department of Mathematics, ²Department of Computing
Imperial College London, London SW7 2AZ, UK

* Both authors contributed equally to this work
<firstname.surname@imperial.ac.uk>

Abstract

In this paper, we propose a new algorithm to compute intrinsic means of organ shapes from 3D medical images. More specifically, we explore the feasibility of Karcher means in the framework of the *large deformations by diffeomorphisms* (LDDMM). This setting preserves the topology of the averaged shapes and has interesting properties to quantitatively describe their anatomical variability. Estimating Karcher means requires to perform multiple registrations between the averaged template image and the set of reference 3D images. Here, we use a recent algorithm based on an optimal control method to satisfy the geodesicity of the deformations at any step of each registration. We also combine this algorithm with organ specific metrics. We demonstrate the efficiency of our methodology with experimental results on different groups of anatomical 3D images. We also extensively discuss the convergence of our method and the bias due to the initial guess. A direct perspective of this work is the computation of 3D+time atlases.

1 Introduction

In the field of *Computational Anatomy* [Grenander and Miller, 1998, Pennec, 2009, Younes et al., 2009], the analytical and statistical study of biological shape variability has been actively developed in the past fifteen years. In this context, the Riemannian point of view on shape spaces has provided efficient tools [Pennec, 2006, Miller et al., 2002, 2006, Younes et al., 2008, Twinings et al., 2002] allowing the use of powerful statistical methods developed for Riemannian manifolds [Fletcher et al., 2004, 2008]. The driving motivation of this work is to quantify, on real 3D images, the anatomical variability of biological shape populations, with a particular attention to the topology preservation of the organs. We therefore

study a topology preserving method for averaging biological shapes that can be extended to spatio-temporal data. For biomedical data like 3D cerebral images for instance, preserving the structures topology is a key challenge when registering or averaging images. This is due to the large anatomical variability of these organs. Diffeomorphic techniques are then of considerable interest since they can encode large deformations while preserving the shape topology. Defining an average shape in a diffeomorphic framework has been addressed in several works, using deterministic [Beg and Khan, 2006, Avants and Gee, 2004, Jia et al., 2010] or Bayesian approaches [Ma et al., 2008, Sabuncu et al., 2009]. Mixed methods using intensity voxel averaging and diffeomorphic registration have also been developed in [Joshi et al., 2004] and extended to spatio-temporal averaging. The averaging method of [Joshi et al., 2004] does not however preserve the shape topology, since it mixes two averaging strategies, which are the Karcher mean [Karcher, 1977, Fletcher et al., 2004], *i.e.* intrinsic mean on Riemannian manifold, and an extrinsic mean as explained in [Fletcher et al., 2004]. In this work, we study the strategy of [Pennec, 2006, Fletcher et al., 2008] to compute the Karcher mean on images using the framework of *large deformations by diffeomorphisms* (LDDMM) [Lorenzen et al., 2005, Beg et al., 2005, Glaunès et al., 2004]. The Karcher averaging method has been tested in different contexts for biomedical data such as [Joshi et al., 2010], where it is used on sulcal lines. Compared with [Pennec, 2006, Fletcher et al., 2008], the novelty of our study is that we use this strategy on segmented 3D medical images requiring large deformations. Importantly, we make use of a new technique to register image pairs, as described below and we also make use of special metrics which allow to take into account organ specific properties when averaging shapes.

The LDDMM framework is a versatile Riemannian setting to match shapes of interest using diffeomorphisms [Beg et al., 2005]. The main idea underlying this framework is to act on the shape space via a group of diffeomorphisms, which induces a Riemannian metric on the shape spaces. Registering images or estimating an average shape reduce to computing geodesics on this shape space. More precisely, the gradient descent algorithm to compute Karcher mean described in [Fletcher et al., 2008, Pennec, 2006] relies on the computation of the initial tangent vector defining the geodesic under the exponential map. In the LDDMM framework, the usual method [Beg et al., 2005, Beg and Khan, 2006] estimates the whole geodesic but the initial tangent vector does not properly encode the geodesic path when the registration has not entirely converged. This convergence is however often truncated to keep the computational burden reasonable. In this work, we then use a new efficient algorithm to accurately estimate geodesics and their initial tangent vector in the LDDMM framework. This algorithm uses optimal control methods to optimise only over the geodesic flow on the space of shapes. The present paper extends the work previously presented in [Vialard et al., 2011a]. In addition to the ideas developed in [Vialard et al., 2011a], we give here thorough explanations about the LDDMM framework and the geodesic equations. We also justify the multi-scale metrics we used. In our tests, we finally present a new result on the algorithm convergence which was obtained on three types of shapes.

We present the LDDMM framework and the geodesic shooting registration algorithm in Section 2 and Section 3 respectively. The methodology to define the intrinsic mean is exposed in Section 4 and then the important choice of the metric underlying the LDDMM setting is discussed in Section 5. Section 6 presents a detailed study of the proposed methodology on three different groups of biomedical images. Future works are finally discussed in section 7.

2 Large deformation by diffeomorphisms framework

In the context of *large deformations by diffeomorphisms* [Dupuis et al., 1998, Joshi and Miller, 2000, Beg et al., 2005], the registration between two scalar images I and J defined on a domain Ω consists in the minimisation of the functional

$$\mathcal{E}(v) \doteq \frac{1}{2} \int_0^1 \|v_t\|_V^2 dt + \|I \circ \phi_{0,1}^{-1} - J\|_{L^2}^2, \quad (1)$$

where $u \in L^2([0, 1], V)$ is a time-dependent velocity field and the space V is usually a Reproducing Kernel Hilbert Space of smooth vector fields defined on Ω . In practice, V is usually chosen as a Sobolev space of sufficiently high-order [Joshi et al., 2004, Beg and Khan, 2006] for 3D image registration. The deformation $\phi_{0,1}$ is generated by the ODE, setting $t = 0$: $\frac{d}{ds}\phi_{t,s} = v_s \circ \phi_{t,s}$, where $\phi_{t,t} = Id$. The first term of the functional \mathcal{E} represents the energy of the time-dependent velocity field. A well-known property of this approach is that it induces right-invariant metric on the group of diffeomorphisms as well as a Riemannian metric on the orbit of the image I , *i.e.* the set of all deformed images by the registration algorithm. However, due to possible topological discrepancy between images, it does not induce a Riemannian metric on the whole space of images. This would require a different approach like metamorphoses, for instance [Trouvé and Younes, 2005, Holm et al., 2009]. Denoting $I_t = I \circ \phi_{t,0}$ and $J_t = J \circ \phi_{t,1}$, the Euler-Lagrange equation associated with (1) reads $v_t = K \star \left(\text{Jac}(\phi_{t,1}^v) \nabla I_t (I_t - J_t) \right)$, where K is the translation-invariant smooth kernel associated with V , \star denotes the convolution operator and Jac is the Jacobian. This equation can be rewritten as

$$\begin{cases} \partial_t I_t + \nabla I_t \cdot v_t = 0, \\ \partial_t P_t + \nabla \cdot (P_t v_t) = 0, \\ v_t + K \star \nabla I_t P_t = 0, \end{cases} \quad (2)$$

where P_t is the so-called momentum variable at time t , which is defined as $P_t = \text{Jac}(\phi_{t,1}^v)(I_t - J_t)$. Interestingly, the system (2) can be integrated once given P_0 the initial momentum. The optimal paths for (1) are then geodesics on the orbit of the source image I_0 , which are completely encoded in this initial momentum P_0 . A gradient descent on the functional \mathcal{E} is the standard approach to numerically solve the matching problem [Beg et al., 2005, Joshi et al., 2004]. In several papers [Singh et al., 2010, Beg and Khan, 2006], the shooting property of the optimised path is used to build average shapes or to perform statistics on this initial momentum. However, obtaining a geodesic path by using this gradient descent may require a large number of iterations. In practice, the estimated initial momentum from [Beg et al., 2005] may not accurately encode the final diffeomorphism, unless the underlying deformation is small. As a consequence, an accurate estimation of the initial momentum will reinforce the statistical power of approaches such as in [Singh et al., 2010, Vaillant et al., 2004]. In the next section, we propose a new methodology to perform an estimation of the initial momentum that is coherent with the shooting scheme used to compute geodesics. In other words, the optimal deformation is computed using the shooting method on the optimal initial momentum.

3 Optimal control for geodesic shooting

The minimisation of the functional \mathcal{E} can be carried over the geodesic flow, which leads to the minimisation of

$$\mathcal{S}(P_0) = \frac{\lambda}{2} \langle \nabla I_0 P_0, K \star \nabla I_0 P_0 \rangle_{L^2} + \frac{1}{2} \|I_1 - J\|_{L^2}^2, \quad (3)$$

subject to the shooting system (2) with initial condition P_0 for the initial momentum. Note that the final diffeomorphism does not appear any more in this formulation, contrary to (1).

In order to compute the gradient of (3), we follow an optimal control approach: We introduce a time-dependent Lagrange multiplier to constrain the paths to be geodesics. We then obtain

Theorem 1 *The gradient of \mathcal{S} is given by:*

$$\nabla_{P_0} \mathcal{S} = -\hat{P}_t + \lambda \nabla I_t \cdot K \star (P_0 \nabla I_0)$$

where \hat{P}_0 is given by the solution of the following PDE solved backward in time:

$$\begin{cases} \partial_t \hat{I}_t + \nabla \cdot (v_t \hat{I}_t) + \nabla \cdot (P_t \hat{v}_t) = 0, \\ \partial_t \hat{P}_t + v_t \cdot \nabla \hat{P}_t - \nabla I_t \cdot \hat{v}_t = 0, \\ \hat{v}_t + K \star (\hat{I}_t \nabla I_t - P_t \nabla \hat{P}_t) = 0, \end{cases} \quad (4)$$

subject to the initial conditions $\hat{I}_1 = J - I_1$ and $\hat{P}_1 = 0$ and that P_t, I_t are the solution of the shooting system (2) for the initial conditions I_0, P_0 .

Existence of the geodesic flow (2) and the solutions to the adjoint equations (4) can be proven, provided that the source and target images are sufficiently smooth, namely H^2 . The algorithm to compute the gradient is divided into two steps: First, solving the shooting system (2) forward from the initial conditions I_0, P_0 ; second, solving backward the adjoint equations (4). The calculation of the adjoint equations can be done efficiently via an integral formulation. We used in our experiments a simple gradient descent approach for the optimisation. Details of the algorithm and its mathematical justification are developed in [Vialard et al., 2011b]. We recall that the key difference between the standard LDDMM implementation of [Beg et al., 2005] and the geodesic strategy of [Vialard et al., 2011b] is that the deformations of [Vialard et al., 2011b] satisfy the geodesic flow equations (2) at each step although this property is only respected at convergence using [Vialard et al., 2011b]. This property is crucial to properly estimate Karcher means.

4 Karcher mean

We use the methodology of [Pennec, 2006, Fletcher et al., 2004] to define the average of a group of images having the same topology. Given a group of imaged shapes I^1, \dots, I^n and a Riemannian metric d on the images, an average can be defined as a minimiser of

$$\mathcal{M}(I) = \frac{1}{2n} \sum_{k=1}^n d(I, I^k)^2. \quad (5)$$

Note that the uniqueness is not guaranteed in general. However, in finite dimensions it can be proven that if the group of data lies in a sufficiently small neighbourhood, there exists a unique minimiser to (5). As mentioned in Section 2, the matching functional (3) does not give a geodesic distance between two images, but between the template and its deformed image. We then approximate the functional (5) by

$$\mathcal{M}(I) \approx \frac{1}{2n} \sum_{k=1}^n d(I, I_1^k)^2, \quad (6)$$

where I_1^k is the result of the shooting equations for the initial condition $P_0 = P_0^k$ and P_0^k is a minimiser of the matching functional (3) for $J = I^k$. In this case, the squared distance is given $\langle \nabla I P_0, K \star (\nabla I P_0) \rangle_{L^2}$ and the gradient of \mathcal{M} is given by

$$\nabla \mathcal{M}(I) = -\frac{1}{n} \sum_{k=1}^n K \star \nabla I P_0^k, \quad (7)$$

where P_0^k is the initial momentum matching I on I^k via the shooting system (2). In particular, at an average shape I^{mean} , the gradient of \mathcal{M} vanishes. In that situation, the gradient is given by (7). The intrinsic mean is given by a gradient descent procedure:

Algorithm 1 *Input:* I^1, \dots, I^n

Output: T the average template

Initialise $T^0 = I^1, \varepsilon > 0$ and $\alpha > 0$.

While $\langle \nabla T^i P^{mean}, K \star \nabla T^i P^{mean} \rangle_{L^2} > \varepsilon$

1. Register T^i on each I^k for $k \in [1, n]$ with geodesic shooting and extract P_0^k the corresponding initial momentum.
2. Compute $P^{mean} = \frac{\alpha}{n} \sum_{k=1}^n P_0^k$.
3. Compute I_1 from (4) with initial conditions $I_0 = T^i$ and $P_0 = P^{mean}$ and update $T^{i+1} = I_1$.

The convergence of this algorithm can be assessed via the norm of the momentum P_{mean} . When the squared norm is smaller than the threshold ε , the algorithm stops. Importantly, this algorithm relies on the estimation of the initial momentum P_0 when registering two images and is therefore sensitive to its accuracy.

The choice of the initial guess for the intrinsic mean is important, and is therefore discussed in Section 6.3. Note that in our context, the computational cost of determining the distances for all image pairs is too expensive. Hence, localising the mean as developed in [Xie et al., 2010] cannot be readily applied in our context. However, their methodology could be interestingly adapted when dealing with a large number of images. Indeed, in that case, many local minima to the functional (6) could occur and localising the mean would be crucial. In the next section, we discuss the choice of the kernel K that defines the Riemannian metric, on which the Karcher mean depends, on the space of images.

5 Metric definition

In the LDDMM framework, the metric on the space of diffeomorphism is determined by the kernel K . The choice of K is particularly important as it directly controls smoothness and/or

preferential orientation of the estimated deformations. Most approaches use isotropic Gaussian kernels or kernels having a very small extent in space. A wide family of kernels K is nevertheless available. In order to account for the anatomical specificities of the averaged organs, we perform shape comparisons using the versatile multi-kernel approach of [Risser et al., 2011]. The notion of characteristic scale is at the heart of the paper. It defines the scale at which image features are typically deformed. Feature differences at a smaller scale cannot therefore be captured and differences at a larger scale might be captured with non-natural transformations due to the little regularisation. When feature differences are observed at several scales simultaneously, we define the multi-kernels MK as the sum of N isotropic Gaussian kernels K_n , each of them having a standard deviation σ_n which represents a characteristic scale: $MK = \sum_{n=1}^N a_n \mathcal{N}(0, \sigma_n)$. Insights about the tuning of the weights a_n are developed in [Risser et al., 2011]. Using this formulation, the estimated momenta can therefore encode multi-scale information. Note that these multi-scale metrics also contribute to robustify the geodesic shooting algorithm as discussed in [Vialard et al., 2011b].

6 Applications

6.1 Experimental data and parameters

The motivation of this work is to estimate average organ shapes and their variability in the LDDMM framework from a set of reference imaged organs. The goal is then to detect anatomical abnormalities from the initial momenta between the average shape and test imaged organs. We therefore test here the ability of our algorithm to estimate average shapes for different groups of 3D imaged organs:

- We first estimate the average shape of segmented hippocampal images out of the Alzheimer’s Disease Neuroimaging Initiative (ADNI) study [Mueller et al., 2005, Jack et al., 2008, Schuff et al., 2009]. We randomly selected eight healthy controls. All T1-weighted 1.5T MR-images were then pre-processed and segmented using the standard ADNI pipeline [Jack et al., 2008].
- Our methodology is also applied to eight 3D MR brain scans acquired on several preterm infants between 29 and 31 weeks of gestational age. The brain scans were acquired with a spatial resolution of 0.85mm. Bias field correction was first performed using N3 [Sled et al., 1998] and the images were rigidly aligned. We then performed the probabilistic segmentation of the brain grey matter using the method of [Murgasova et al., 2011].
- We finally consider eight other 3D MR brain scans pre-treated with the same protocol, but acquired on preterm infants between 37 and 39 weeks of gestational age.

As shown in Fig. 1, these three image groups have different levels of complexity. While the hippocampi can be registered using only small deformations, large deformations are obviously required to match the 38 weeks old cortices. The 30 weeks brains also require intermediate deformations. We then denote in all tests R^n , $n \in [1, \dots, N]$ the reference images and A_i^n the average image estimate after i iterations, where $A_0^n = R^n$. For the sake of simplicity, we use here reference images as initial guesses of the average images.

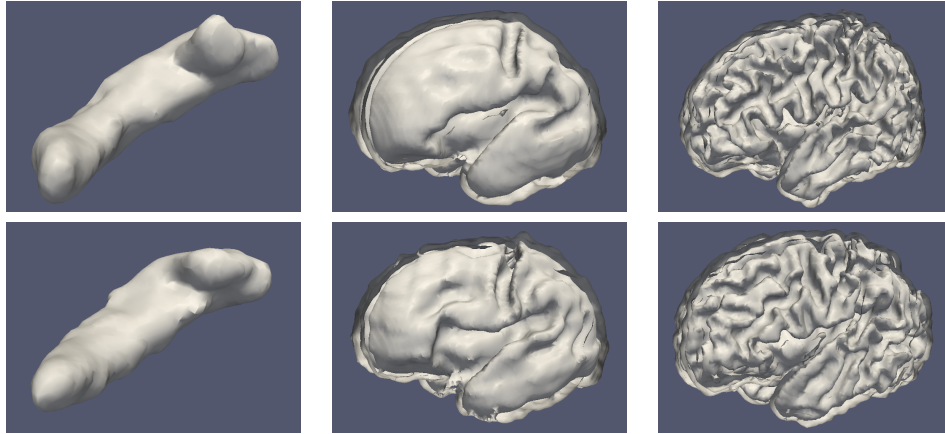


Figure 1: Isosurface of typical segmented 3D MR images from which the average shapes are estimated. **(Left)** Isosurface of hippocampi. **(Centre)** Internal face of cortical surfaces out of two pre-term babies acquired at 29 and 31 weeks of gestational age. **(Right)** Internal face of cortical surfaces out of two pre-term babies acquired at 38 and 38.5 weeks of gestational age.

We discussed in section 5 the importance of the metric when estimating an average shape using the proposed strategy. Here, we use a simple Gaussian kernel K with a standard deviation of 1mm when registering hippocampi. For the brains, we characterise feature differences at several scales simultaneously, by using the multi-kernel technique of [Risser et al., 2011]. At least two scales can be reasonably distinguished to quantify anatomically inter-subject brain variability: A large scale, related to the general skull anatomy and a smaller one, related to the shape of the sulci. We then define for the brains the kernel K as the sum of two isotropic Gaussian kernels of standard deviation 25mm and 1.5mm. Note that we not only perform a multi-scale strategy according to the kernels K but also multi-resolution registration method. At a coarse resolution, we only use a Gaussian kernel of standard deviation 25mm subsampled with the same factor as the images, while at full resolution the multi-kernel is fully considered.

6.2 Convergence of the initial momentum

A property of the proposed technique is that the average value \hat{P}_0 of the initial momenta P_0^n , encoding the deformation from an average image estimate A_i^m to the reference image R^n , is null everywhere in Ω after convergence of the algorithm. We then show the behaviour of this convergence for the three organ groups defined in the previous subsection. To do so, we show in Fig. 2 (left), the norm of the average momenta \hat{P}_0 iteration after iteration. Note that these norms are normalised to 1 at the first iteration for each organ group. As expected, the norms decrease iteration after iteration for all organs. Interestingly, the convergence is strong from the first iteration of the algorithm. Note that the variability of the initial shapes is smaller for the hippocampi than the cortices. The convergence therefore appears slower in that case since the curves are normalised and few deformations are required.

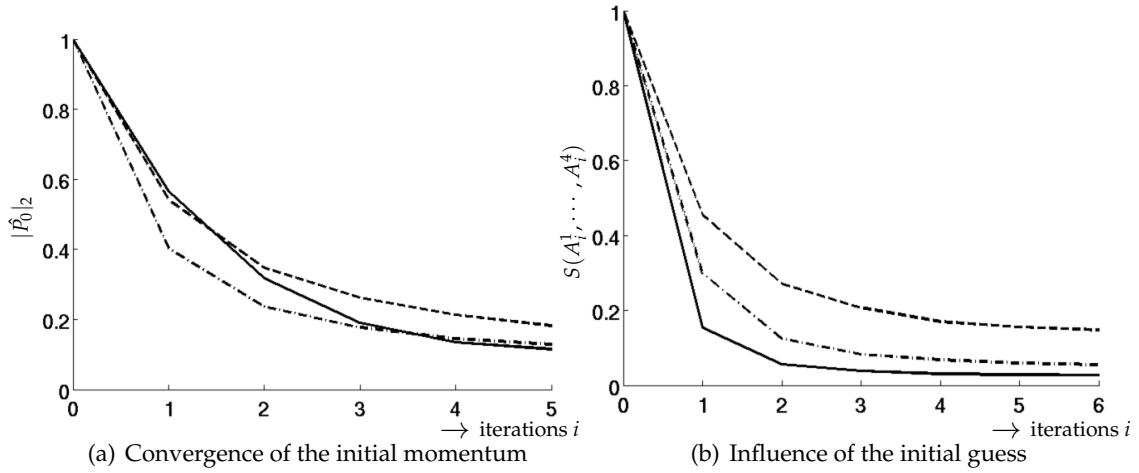


Figure 2: **(a)** Norm of \hat{P}_0 , i.e. the average of the initial momenta P_0^n which encode the deformation from the average image estimate A_i^m to the reference images R^n . Each A_0^m is randomly selected among the reference images for each organ group. **(b)** Similarity $S(A_i^1, \dots, A_i^4)$ of the average estimates A_i^m for four different initial guesses m (see subsection 6.3). **(a-b)** The norms and similarities are function of the iteration number i for the hippocampi (continuous line), the 30 weeks brains (semi dashed line) and the 38 weeks brains (dashed line).

6.3 Influence of the initial guess

We now discuss an important point to validate our methodology: the influence of the initial guess. For a set of reference shapes and an initial guess, the algorithm converges toward an optimal average shape. However, there is no uniqueness of the optimised shape for different initial guesses. We then measure here the similarity of the average shape estimates using different initial guesses. In each distinguished reference image dataset R^n , $n \in [1, \dots, N]$, we pick up 4 different initial guesses and perform average shape estimations. In Fig. 3, we show the evolution of the 3D images of 30 weeks old cortices in a 2D slice during the 3 first iterations. In order to quantify the similarity of the different images, we also measure $S(A_i^1, \dots, A_i^4) = \frac{1}{16} \sum_{m=1}^4 \sum_{p=1}^4 SSD(A_i^m, A_i^p)$, where $SSD(.,.)$ is the sum of squared differences between two images. If S is null, then the average estimates are all the same and the higher this value, the more different are the images. Results are given in Fig. 2 (right).

In all the considered cases, the average estimates are increasingly similar. Interestingly, the influence of the initial guess is very weak after only one iteration for the hippocampi and a few iterations for the 30 weeks old brains as shown Fig. 3. The convergence is however slower for the more complex 38 years old brain. We can indeed observe in Fig. 2 (right) that while about 85% of the differences are lost in one iteration for the hippocampi and two iterations for the 30 weeks old brains, five iterations are needed for the 38 weeks old brains for a similar result. This number of iterations remains however limited regarding the differences in the initial guesses. The proposed methodology therefore appears efficient to estimate average shapes but requires an increasingly number of iterations according to the complexity of the reference shapes.

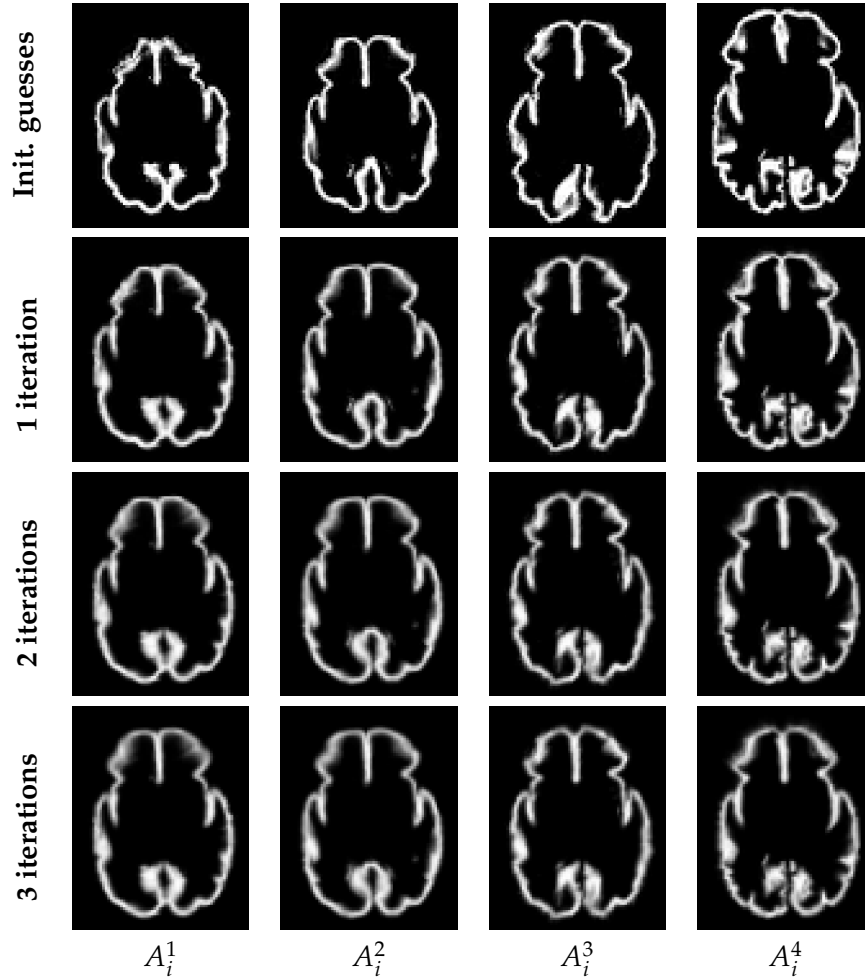


Figure 3: Average image estimates A_i^m , $m \in \{1, \dots, 4\}$ after $i = 0, 1, 2$ and 3 iterations, where m represents the identifier of the initial guess. Here the evolution of the 3D shapes of 30 weeks old cortices are shown in a 2D slice.

7 Outlook

In this work, we have successfully explored the Karcher mean strategy of [Pennec, 2006, Fletcher et al., 2008] in a diffeomorphic setting, to estimate average shapes on 3D medical images requiring large deformations. To this end, our main contribution is to use a new diffeomorphic technique within the LDDMM framework combined with organ specific metrics to compare image pairs. The whole averaging strategy therefore preserves the shape topology even for organs having a large variability and it does not require intensity averaging. We have also shown that the algorithm computes good estimates of the averaged shapes in very few iterations for shapes requiring small deformations and a limited number of iterations for more complex shapes. It is also not that much dependent on the initial guess after a sufficient number of iterations, which increases with the anatomical complexity of the reference shapes. The immediate perspective of this work is to estimate temporal atlases of the early cortical growth. Other potential directions consist in performing descriptive and inferential

statistics on 3D and 3D+t shape populations.

Acknowledgement

The authors thank the Imperial College Strategic Initiative Fund for partial support. They are grateful to Alain Trouvé, Xavier Pennec, Martins Bruveris and Franck Plouraboué for constructive discussions. The work of DDH was partially supported by the Royal Society of London Wolfson Research Merit Award and the European Research Council Advanced Investigator Grant. LR partially worked on this paper during his Post-doctorate at University of Oxford, Institute for Biomedical Engineering.

References

- B. Avants and J. Gee. Shape averaging with diffeomorphic flows for atlas creation. In *IEEE Int. Symposium on Biomedical Imaging*, 2004.
- M. F. Beg, M. I. Miller, A. Trouvé, and L. Younes. Computing large deformation metric mappings via geodesic flow of diffeomorphisms. *Int. Journal of Computer Vision*, 61:139–157, 2005.
- M. F. Beg and A. Khan. Computing an average anatomical atlas using LDDMM and geodesic shooting. In *IEEE Int. Symposium on Biomedical Imaging*, pages 1116–1119, 2006.
- P. Dupuis, U. Grenander, and M. I. Miller. Variational problems on flows of diffeomorphisms for image matching. *Quarterly of Applied Mathematics*, LVI(3):587–600, 1998.
- P. T. Fletcher, C. Lu, M. Pizer, and S. Joshi. Principal geodesic analysis for the study of nonlinear statistics of shape. *IEEE Trans. on Medical Imaging*, pages 995–1005, 2004.
- P. T. Fletcher, S. Venkatasubramanian, and S. Joshi. Robust statistics on Riemannian manifolds via the geometric median. In *Computer Vision and Pattern Recognition*, pages 1–8, 2008.
- J. Glaunès, M. Vaillant, and M. I. Miller. Landmark matching via large deformation diffeomorphisms on the sphere. *Journal of Mathematical Imaging and Vision*, 20:179–200, 2004.
- U. Grenander and M. I. Miller. Computational Anatomy: An emerging discipline. *Quarterly of Applied Mathematics*, LVI(4):617–694, 1998.
- D. D. Holm, A. Trouvé, and L. Younes. The Euler-Poincare theory of Metamorphosis. *Quarterly of Applied Mathematics*, 67:661–685, 2009.
- C. R. Jack, M. A. Bernstein, N. C. Fox, P. Thompson, G. Alexander, D. Harvey, B. Borowski, P. J. Britson, J. L. Whitwell, C. Ward, A. M. Dale, J. P. Felmlee, J. L. Gunter, D. L. Hill, R. Kiliany, N. Schuff, S. Fox-Bosetti, C. Lin, C. Studholme, C. S. DeCarli, G. Krueger, H. A. Ward, G. J. Metzger, K. T. Scott, R. Mallozzi, D. Blezek, J. Levy, J. P. Debbins, A. S. Fleisher, M. Albert, R. Green, G. Bartzokis, G. Glover, J. Mugler, and M. W. Weiner. The Alzheimer’s Disease Neuroimaging Initiative (ADNI): MRI methods. *Journal of Magnetic Resonance Imaging*, 27(4):685 – 691, 2008.

- H. Jia, G. Wu, Q. Wang, and D. Shen. ABSORB: Atlas building by self-organized registration and bundling. In *Computer Vision and Pattern Recognition*, pages 2785–2790, 2010.
- S. Joshi, B. Davis, M. Jomier, and G. Gerig. Unbiased diffeomorphic atlas construction for computational anatomy. *NeuroImage*, 23:151–160, 2004.
- S. H. Joshi, R. P. Cabeen, A. A. Joshi, R. P. Woods, K. L. Narr, and A. W. Toga. Diffeomorphic sulcal shape analysis for cortical surface registration. In *Computer Vision and Pattern Recognition*, pages 475–482, 2010.
- S. Joshi and M. I. Miller. Landmark matching via large deformation diffeomorphisms. *IEEE Trans. on Image Processing*, 9(8):1357–1370, aug. 2000.
- H. Karcher. Riemannian center of mass and mollifier smoothing. *Communications on Pure and Applied Mathematics*, 30(5):509–541, 1977.
- P. Lorenzen, B. Davis, and S. Joshi. Unbiased atlas formation via large deformations metric mapping. In *Int. Conf. on Medical Image Computing and Computer Assisted Intervention*, volume 8, pages 411–418, 2005.
- J. Ma, M. I. Miller, A. Trouvé, and L. Younes. Bayesian template estimation in computational anatomy. *NeuroImage*, 42(1):252–261, 2008.
- M. I. Miller, A. Trouvé, and L. Younes. On the metrics and Euler-Lagrange equations of computational anatomy. *Annual Review of biomedical Engineering*, 4:375–405, 2002.
- M. I. Miller, A. Trouvé, and L. Younes. Geodesic shooting for computational anatomy. *Journal of Mathematical Imaging and Vision*, 24(2):209–228, 2006.
- S. G. Mueller, M. W. Weiner, L. J. Thal, R. C. Petersen, C. Jack, W. Jagust, J. Q. Trojanowski, A. W. Toga, and L. Beckett. The Alzheimer’s disease neuroimaging initiative. *Neuroimaging Clinics of North America*, 15(4):869–877, 2005.
- M. Murgasova, P. Aljabar, L. Srinivasan, S. J. Counsell, V. Doria, A. Serag, I. S. Gousias, J. P. Boardman, M. A. Rutherford, A. D. Edwards, J. V. Hajnal, and D. Rueckert. A dynamic 4D probabilistic atlas of the developing brain. *NeuroImage*, 54(4):2750–63, 2011.
- X. Pennec. Intrinsic statistics on Riemannian manifolds: Basic tools for geometric measurements. *Journal of Mathematical Imaging and Vision*, 25:127–154, 2006.
- X. Pennec. Statistical computing on manifolds: From Riemannian geometry to computational anatomy. *Emerging Trends in Visual Computing*, 5416:347–386, 2009.
- L. Risser, F. X. Vialard, R. Wolz, M. Murgasova, D. D. Holm, and D. Rueckert. Simultaneous multiscale registration using large deformation diffeomorphic metric mapping. *IEEE Trans. on Medical Imaging*, 2011.
- M. R. Sabuncu, S. K. Balci, M. E. Shenton, and P. Golland. Image-driven population analysis through mixture modeling. *IEEE Trans. on Medical imaging*, 28(9):1473–1487, 2009.

- N. Schuff, N. Woerner, L. Boreta, T. Kornfield, L. M. Shaw, J. Q. Trojanowski, P. M. Thompson, J. C. R. Jack, M. W. Weiner, and the Alzheimer's; Disease Neuroimaging Initiative. MRI of hippocampal volume loss in early Alzheimer's disease in relation to ApoE genotype and biomarkers. *Brain*, 132(4):1067 – 1077, 2009.
- N. Singh, P. T. Fletcher, J. S. Preston, L. Ha, R. King, J. S. Marron, M. Wiener, and S. Joshi. Multivariate statistical analysis of deformation momenta relating anatomical shape to neuropsychological measures. In *Int. Conf. on Medical Image Computing and Computer Assisted Intervention*, 529–537. 2010.
- J. G. Sled, A. P. Zijdenbos, and A. C. Evans. A nonparametric method for automatic correction of intensity nonuniformity in MRI data. *IEEE Trans. on Medical Imaging*, 17(1):87–97, 1998.
- A. Trounev and L. Younes. Metamorphoses through lie group action. *Foundations of Computational Mathematics*, 5(2):173–198, 2005.
- C. Twinings, S. Marsland, and C. Taylor. Measuring geodesic distances on the space of bounded diffeomorphisms. In *British Machine Vision Conference*, 2002.
- M. Vaillant, M. I. Miller, A. Trounev, and L. Younes. Statistics on diffeomorphisms via tangent space representations. *NeuroImage*, 23(S1):S161–S169, 2004.
- F. X. Vialard, L. Risser, D. D. Holm, and D. Rueckert. Diffeomorphic atlas estimation using Karcher mean and geodesic shooting on volumetric images. In *Medical Image Understanding and Analysis*, 2011.
- F. X. Vialard, L. Risser, D. Rueckert, and C. J. Cotter. Diffeomorphic 3D image registration via geodesic shooting using an efficient adjoint calculation. *Int. Journal of Computer Vision*, 2011.
- Y. Xie, J. Ho, and B. C. Vemuri. Image atlas construction via intrinsic averaging on the manifold of images. *Computer Vision and Pattern Recognition*, pages 2933 –2939, 2010.
- L. Younes, P. Michor, J. Shah, and D. Mumford. A metric on shape spaces with explicit geodesics. *Rendiconti Lincei - Matematicae e Applicazioni*, 9:25–57, 2008.
- L. Younes, F. Arrate, and M. I. Miller. Evolutions equations in computational anatomy. *NeuroImage*, 45(1, Supplement 1):S40 – S50, 2009.